Ultralow-threshold, Continuous-wave Upconverting Lasing from Sub-wavelength Plasmons

Angel Fernandez-Bravo[†1], Danqing Wang[†2], Edward S. Barnard[1], Ayelet Teitelboim[1], Cheryl Tajon[1], Jun Guan[2], George C. Schatz[2,5], Bruce E. Cohen[1], Emory M. Chan[1], P. James Schuck*[1,3] and Teri W. Odom*[2,4,5]

[1]The Molecular Foundry, Lawrence Berkeley National Laboratory, Berkeley, California 94720 USA

[2]Graduate Program in Applied Physics, Northwestern University, Evanston, Illinois 60208 USA

[3]Department of Mechanical Engineering, Columbia University, New York, New York 10027 USA

[4]Department of Materials Science and Engineering, Northwestern University, Evanston, Illinois 60208 USA

[5]Department of Chemistry, Northwestern University, Evanston, Illinois 60208 USA

[†]equal contributions

Correspondence to: p.j.schuck@columbia.edu; todom@northwestern.edu

Miniaturized lasers are an emerging platform for generating coherent light for quantum photonics, in-vivo cellular imaging, solid-state lighting, and fast 3D sensing in smartphones[1-3]. Continuous-wave (CW) lasing at room temperature is critical for integration with opto-electronic devices and optimal modulation of optical interactions[4,5]. Plasmonic nanocavities integrated with gain can generate coherent light at sub-wavelength scales[6-9], beyond the diffraction limit that constrains mode volumes in dielectric cavities such as semiconducting nanowires[10,11]. However, insufficient gain

with respect to losses and thermal instabilities in nanocavities has limited all nanoscale lasers to pulsed pump sources and/or low-temperature operation[6-9,12-15]. Here we show CW upconverting lasing at room temperature with record-low thresholds and high photostability from sub-wavelength plasmons. We achieve selective, single-mode lasing from Yb^{3+}/Er^{3+}-co-doped upconverting nanoparticles (UCNPs) conformally coated on Ag nanopillar arrays that support a single, sharp lattice plasmon cavity mode and < λ/20 field confinement in the vertical dimension. The intense electromagnetic near-fields localized in the vicinity of the nanopillars result in a threshold of 70 W/cm^2, orders of magnitude lower than other small lasers. Our plasmon-nanoarray upconverting lasers provide directional, ultra-stable output at visible frequencies under near-infrared pumping, even after six hours of constant operation, which offers prospects in previously unrealizable applications of coherent nanoscale light.

Lanthanide-based UCNPs are photostable solid-state nonlinear emitters that are efficient at sequentially absorbing multiple near-infrared (NIR) photons and emitting at visible and shorter-NIR wavelengths[16-19]. Recently, UCNPs have been used as gain media in small lasers, and their integration with dielectric microcavities and hyperbolic metamaterials has resulted in multi-wavelength upconverted lasing[20-22]. UCNPs also exhibit long radiative lifetimes (typically 100s of μs) compared to other gain materials[18,23,24], which

leads to low saturation intensities that could facilitate CW pumping and population inversion build-up. Pump powers required for UCNP lasing are orders of magnitude lower than those for nanolasers based on quantum dots, dye molecules, or conventional nonlinear optical materials[7,22,25]. Additionally, organic molecules exhibit triplet-state accumulation and limited photostability, and semiconductor nanomaterials undergo Auger recombination, which reduces population inversion under CW pump[4,26,27].

Multiphoton upconverting processes can be strongly enhanced by the intense electromagnetic fields from plasmonic nanostructures[28]. However, surface plasmon resonances from single nanoparticles are typically broadband with low mode quality. Spectral overlap with multiple, narrow UCNP energy bands results in reduced output efficiency at a single targeted mode because of internal energy transfer[29,30]. Arrays of metal nanoparticles can overcome these challenges because collective, coherent coupling can produce narrow lattice plasmon resonances (linewidths < 5 nm) with suppressed radiative loss and stronger near-field enhancements compared to single nanoparticles[31,32]. Previously, we demonstrated band-edge lattice plasmons as optical feedback for down-shifted dye nanolasing at room temperature with directional emission and tunable wavelengths[6,7,33,34]. Compared to photonic microcavities that exhibit multiple cavity modes[21], plasmonic nanocavity arrays with a single lattice spacing support a single, narrow mode that can, in principle, selectively enhance specific upconverting energy transitions.

We designed plasmon lasers that integrate two key advances in order to enhance coupling between the nanocavity and the lanthanide (Ln) emitters, to lower upconverting lasing thresholds, and to improve device stability. First, we fabricated Ag nanopillar arrays with a lattice plasmon resonance that overlaps the red Er^{3+} upconverted emission transition ($^4F_{9/2}$ to $^4I_{15/2}$) in colloidal UCNPs doped with sensitizer Yb^{3+} ions / emitter Er^{3+} ions (**Figs. 1a-c**). Second, we exploited core-shell UCNPs with high Ln content that are known to show significantly improved luminescence properties and considerably reduced saturation intensities compared to canonical compositions[24,35-37]. The high-Ln-content UCNPs are core-shell heterostructures with 13.9 ± 1.3 nm diameters comprised of 9.9-nm β-phase $NaYF_4$ cores doped with 20% Yb^{3+} / 20% Er^{3+} and 2-nm $NaYF_4$ shells (Methods, Supplementary Fig. 1)[38]. In our all-solid-state system under ambient conditions, NIR pumping at 980 nm can excite Yb^{3+} ions in the UCNPs, which transfer energy to Er^{3+} ions to facilitate upconverted emission at multiple visible and NIR wavelengths, and lattice plasmon modes can be engineered to couple selectively to Er^{3+} emission (red) (**Fig. 1d**).

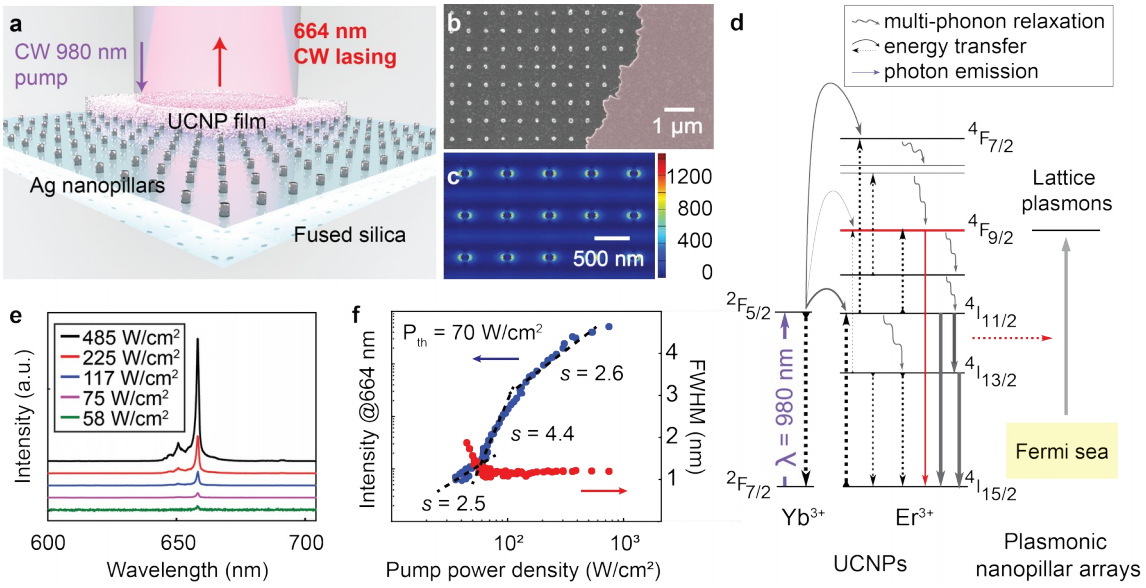

Figure 1. Continuous-wave (CW) upconverting nanolasing on Ag nanopillar arrays at room temperature. a, Schematic of the upconverting nanoparticle (UCNP) coating on top of Ag arrays with spacing a_0 = 450 nm. Ag nanopillars are with 80-nm diameter, 50-nm height and scalable over cm^2 areas. The UCNP film is ca. 150 nm thick. **b**, Scanning electron micrograph showing the Ag nanopillar array with partial conformal coating (right) with a film of 14 nm core-shell UCNPs ($NaYF_4$:Yb^{3+}, Er^{3+}). **c**, Representative near-field $|E|^2$ plot for the 450-nm spaced Ag nanopillars at resonance (n = 1.46) from a finite-difference time-domain method simulation. **d**, Yb^{3+}, Er^{3+} energy levels and coupling mechanism to the lattice plasmons. **e**, Power-dependent lasing spectra from lattice plasmon resonances at λ = 664 nm for Ag nanopillar arrays

The plasmonic arrays consist of Ag nanopillars (80-nm diameter, 50-nm height) arranged in a square lattice with periodicity a_0 ranging from 450 – 460 nm depending on which transition within the Er^{3+} red emission manifold was of interest (Figs. 1a-c). As described previously[31,32], collective coupling of plasmonic nanopillar arrays produces a sharp lattice plasmon mode with a quality factor $Q = \frac{\lambda}{\Delta\lambda}$ > 200 that is maintained after coating with UCNPs

(Supplementary Fig. 2). UCNPs were drop-cast from solution onto the arrays to form conformal films of thickness ca. 150 nm, resulting in UCNPs that are situated at the nanoscale plasmonic hotspots within 25 nm surrounding each nanopillar surface (Figs. 1a-c; near-field enhancement at the nanopillars, $|E|^2/|E_0|^2$ >1000). Since the refractive index n of UCNPs (n ~ 1.47 @ 660 nm) closely matches that of the fused silica substrate (n ~ 1.46 @ 660 nm) (Supplementary Fig. 2), the Ag nanopillars were effectively embedded in a uniform index environment, which is critical for sustaining high-quality lattice plasmons.

To determine whether UCNPs are coupled to the plasmonic nanocavities, we first characterized spontaneous emission from UCNPs on the plasmonic array at low (ca. 20 W/cm^2) pump intensities. Enhanced upconverted emission between 650-660 nm was resolved at each Ag nanopillar position (Supplementary Fig. 3). As CW pump intensity increased beyond a threshold, lasing action occurred at the lattice plasmon resonance wavelength (**Fig. 1e**). At threshold, we observed both a significant increase in rising slope (s = 4.4) in the input-output curve compared to spontaneous emission (s = 2.2; Supplementary Fig. 4) and simultaneous linewidth narrowing of the lasing mode to < 1 nm (**Fig. 1f**, Supplementary Fig. 5, Supplementary Table 1). The measured linewidths above threshold are consistent with those observed in dye-based lattice plasmon lasers[6,7,33]. The lasing threshold of 70 W/cm^2 from the device in Fig. 1 represents a > 200-fold improvement over that of upconverting microresonators[21] and orders of magnitude reduction over that

of nanodisk-on-film[12,39] or nanowire-on-film[14,15] plasmon lasers at room temperature (Supplementary Table 3). The low thresholds of our UCNP plasmon lasers (as low as 29 W/cm^2, Supplementary Fig. 6) can be attributed to both bright Yb^{3+}/Er^{3+}-co-doped UCNPs and single-mode plasmon nanocavities with spectrally selective optical enhancement. The measured external quantum efficiency of 0.04% is consistent with expectations based on Purcell enhancements and known upconverting quantum yield for these UCNPs (Supplementary Figs. 7-8).

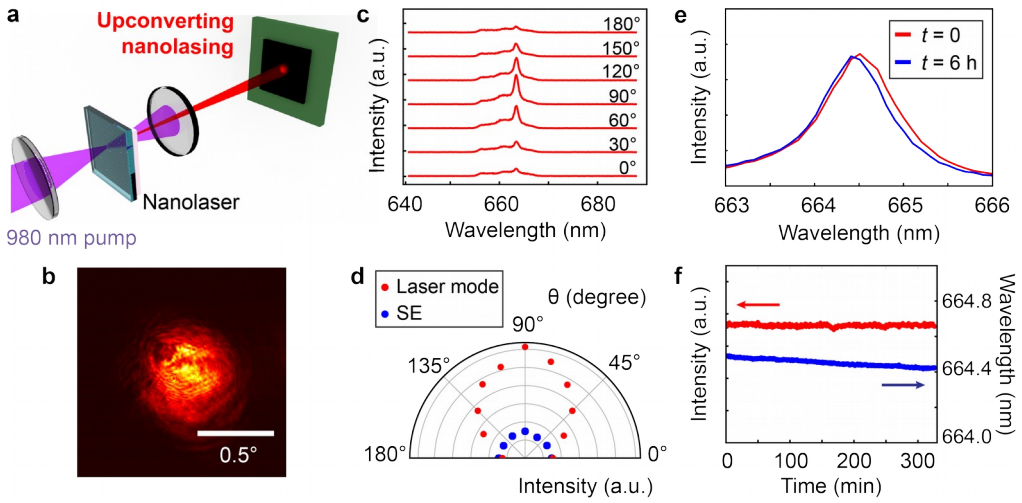

Figure 2. Upconverting nanolasing showed spatial and polarization coherence, as well as high photo-stability. a, Schematic of the experimental optics setup to measure the far-field beam profile. The excitation beam is filtered out using a short pass 745 nm filter and 660/10 nm band pass filter, enabling the CMOS sensor to record only the emission from the plasmon nanolasing at 664 nm. **b**, Far-field beam profile of lasing emission above threshold, with the camera detector placed 2 cm away from the sample plane, showing a beam divergence of ca. 0.5°. **c**, Polarization-dependent lasing emission with pump polarized at 90°. **d**, The polar plot represents the emission intensity of the 664 nm lasing mode and the spontaneous emission (SE) as a function of the

Besides enabling low thresholds, plasmonic array nanocavities offer directional and highly-efficient coupling, in contrast to spherical and cylindrical cavity geometries based on whispering gallery modes, where input coupling is non-trivial and emission is less directional. The collective coupling between periodic Ag nanopillars results in directional, beam-like upconverted emission at the band-edge Γ point[7] with a low divergence angle of ca. 0.5° (**Figs. 2a-b**). Additionally, the lasing beam is polarized along the same direction as the incident pump (**Figs. 2c-d**). This polarization coherence is distinct from unpolarized spontaneous emission from UCNPs

(regardless of excitation polarization) that results from energy transfer migration between dopant ions within a single UCNP over the long lifetimes of Ln^{3+} excited states[23] and random nanocrystal orientation[40]. Moreover, our upconverting nanolaser shows long-term stability, which is typically challenging for multiphoton lasing systems since high peak pump intensities are often required for nonlinear responses[21]. Our all-solid-state system operated at room temperature for more than 6 h under continuous irradiation, the longest operational period we tested (**Figs. 2e-f**). Over this time, we did not observe any optical or thermal damage; the mode intensity remained constant, and only minimal shifts in mode frequency (< 0.15 nm) occurred. In contrast, CW lasing based on semiconductor nanoparticles was not stable over 1 h under fluences similar to those used in this study[4,26].

Interestingly, we find that CW lasing occurs even under pulsed pumping conditions in our upconverting plasmon nanolaser (**Fig. 3**). This observation is consistent with excited state lifetimes that are much longer than both the pulse width and repetition period of the pulsed pump (~120 fs and ~13 ns, respectively). In contrast to measured spontaneous emission lifetimes of ca. 100 μs for these UCNPs[24], the lifetime curve for lasing emission at 660 nm within a 1-μs time window shows a bi-exponential fit with a slower component of 510 ns and a faster component of 66 ns (Supplementary Fig. 9, Supplementary Table 2). These values agree well with our estimated range of Purcell enhancement factors (Supplementary Fig. 8), with increased decay rates for decreased Er^{3+}-nanopillar separation distances. Second-order

correlation measurements ($g^{(2)}(\tau)$) of lasing emission confirm CW output (Supplementary Figs. 10-12). The lasing thresholds under pulsed pumps (in terms of average power) are similar to those under CW pumps (Supplementary Table 3).

To highlight the ability of the system to select specific Er^{3+} transitions for lasing, we varied the nanopillar lattice constant a_0, which modified the lattice plasmon nanocavity mode. Shifting the resonance from 650 nm (a_0 = 450 nm) to 660 nm (a_0 = 460 nm), we observed that the upconverted lasing emission followed the cavity mode resonance, demonstrating that single-mode upconverting lasing is directly determined by the plasmonic nanocavities (**Fig. 3a**). We found similar lasing thresholds and power dependencies for both lattice spacings, including high nonlinearity in the gain portion of the input-output curves (s = 5.3 and 4.7 above the threshold for the devices with modes at 650 nm and 660 nm, respectively, **Fig. 3b**). Note that the extreme saturation of excited states under pulsed excitation led to a smaller rising slope (s = 1.2) at high pump powers.

To gain insight into the lasing mechanisms of these low-threshold upconverting nanolasers, we developed a semi-quantum model and a time-domain approach to study the nonlinear optical build-up under a pulsed pump (**Fig. 3c**). The narrow lattice plasmon resonance provides selective enhancement only for the $^4F_{9/2}$-to-$^4I_{15/2}$ red emission without directly affecting energy transfer processes at other energies. Therefore, we used a simplified

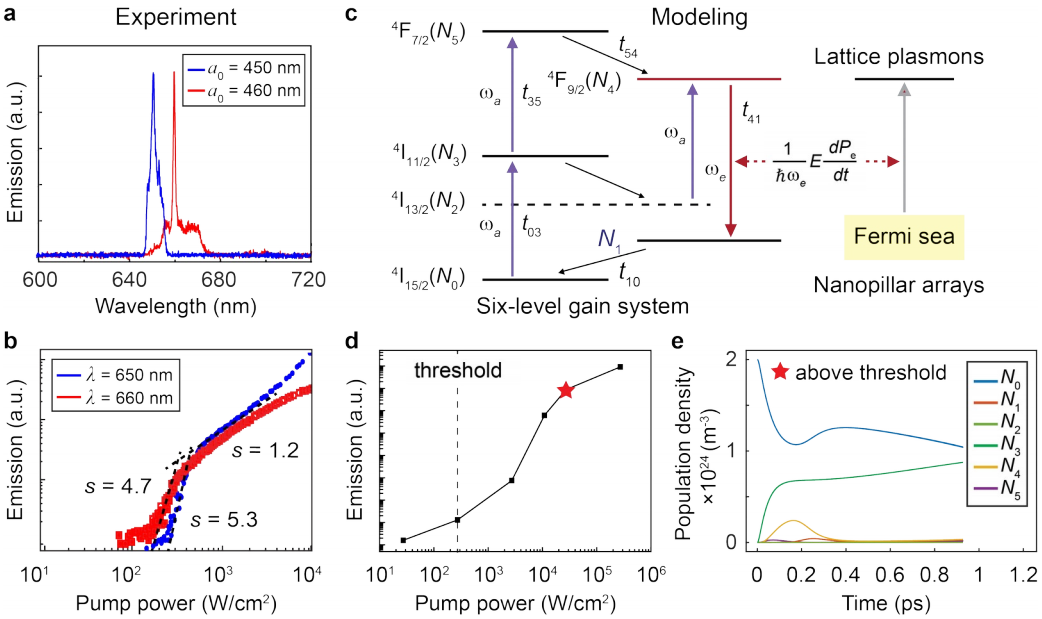

Figure 3. Upconverting CW nanolasing under a pulsed laser and semi-quantum modeling in the time domain. a, Lasing spectra with lasing modes at λ = 650 and 660 nm from UCNPs coupled to Ag nanopillar arrays with spacing a_0 = 450 (blue) and 460 nm (red), respectively. The results show the selective coupling between Er^{3+} red emission from components of the $^4F_{9/2}$ level and the tailored plasmon resonances associated with collective Bragg modes of the Ag nanopillar arrays. **b**, Input-output curves in log-log scale show a slightly lower laser threshold for the mode at 660 nm. **c**, Six-level model system describing upconverting nanolasing and the associated population inversion. The transition lifetimes are $t_{54} = t_{10} = 10$ fs and $t_{41} = 0.1$ ns, respectively, which are reduced to allow for simulation within the computational window (< 3 ps) in the time-domain approach (Supplementary Figs. 13-15). **d**, Simulated input-output curve showing a threshold-like power dependence with laser thresholds comparable to the experimental values. **e**, Simulated time-dependent evolution of population density describing upconverting

six-level model to approximate the multiphoton optical pump process[19], different from the single-photon pump, four-level system[7] for dye-based plasmon nanolasers (Supplementary Fig. 13). The calculations show a large exponentially rising slope (s = 4.8) above the lasing threshold, which is similar to nonlinear buildup seen in the experiments (**Fig. 3d**). In contrast, the slow rise close to threshold (s = 1.8) corresponds to the intrinsic two-photon emission of Yb^{3+}/Er^{3+}-co-doped UCNPs. To capture the time-dependent lasing build-up, we tracked the evolution of population density in different energy levels and found a characteristic population inversion from $^4F_{9/2}$ to $^4I_{15/2}$ above threshold (**Fig. 3e**). No population inversion was observed for upconverted emission below threshold, consistent with a slow rising slope (Supplementary Figs. 14, 15). The calculated lasing threshold occurred at an average power of 270 W/cm^2 (Fig. 3d), comparable with experiments. Minor differences in threshold are likely because of unknown gain values for the UCNPs and the simplified Er^{3+} electronic structure in our model, where we included only select Er^{3+} excited states.

In summary, we demonstrated CW upconverting plasmon nanolasing at room temperature. We observed exceptionally stable lasing over long periods (> 6 h), with lasing thresholds as low as 29 W/cm^2, significantly lower than other plasmon and upconverting nanolasers. In addition, the upconverting nanolaser can achieve CW emission under both CW and pulsed pump conditions. Our time domain, semi-quantum modeling captured the characteristic population inversion and strong optical nonlinearities. Low-

threshold upconverting nanolasers with NIR pump open possibilities for integration with compact, low-power circuits as well as in vivo applications including deep-tissue imaging, sensing, theranostics and optogenetic manipulation[41]. Looking forward, the large variety of available output wavelengths in the Ln series, the ability to couple plasmonic nanocavities with densely-packed quantum emitters, and the general nanocavity architectures provide an almost unlimited number of robust low-power coherent nanoscale light sources. Our all-solid-state nanolaser platform offers prospects to realize quantum-optical technologies and commercial lab-on-a-chip photonic devices.

References

1 Hill, M. T. & Gather, M. C. Advances in small lasers. *Nat Photonics* **8**, 908-918 (2014).

2 Ma, R. M. & Oulton, R. F. Applications of nanolasers. *Nat Nanotechnol* **14**, 12-22 (2019).

3 Wang, D., Wang, W., Knudson, M. P., Schatz, G. C. & Odom, T. W. Structural Engineering in Plasmon Nanolasers. *Chem. Rev.* **118**, 2865-2881 (2017).

4 Fan, F. J. *et al.* Continuous-wave lasing in colloidal quantum dot solids enabled by facet-selective epitaxy. *Nature* **544**, 75-79 (2017).

5 Tamboli, A. C. *et al.* Room-temperature continuous-wave lasing in GaN/InGaN microdisks. *Nat Photonics* **1**, 61-64 (2007).

6 Wang, D. *et al.* Band-edge engineering for controlled multi-modal nanolasing in plasmonic superlattices. *Nat Nanotechnol* **12**, 889-894 (2017).

7 Zhou, W. *et al.* Lasing action in strongly coupled plasmonic nanocavity arrays. *Nat Nanotechnol* **8**, 506-511 (2013).

8 Oulton, R. F. *et al.* Plasmon lasers at deep subwavelength scale. *Nature* **461**, 629-632 (2009).

9 Lu, Y. J. *et al.* Plasmonic nanolaser using epitaxially grown silver film. *Science* **337**, 450-453 (2012).

10 Zhu, H. *et al.* Lead halide perovskite nanowire lasers with low lasing thresholds and high quality factors. *Nat Mater* **14**, 636-642 (2015).

11 Huang, M. H. *et al.* Room-temperature ultraviolet nanowire nanolasers. *Science* **292**, 1897-1899 (2001).

12 Wang, S. *et al.* Unusual scaling laws for plasmonic nanolasers beyond the diffraction limit. *Nature Communications* **8**, 1-8 (2017).

13 Hakala, T. K. *et al.* Lasing in dark and bright modes of a finite-sized plasmonic lattice. *Nature Communications* **8**, 1-7 (2017).

14 Sidiropoulos, T. P. H. *et al.* Ultrafast plasmonic nanowire lasers near the surface plasmon frequency. *Nat Phys* **10**, 870-876 (2014).

15 Zhang, Q. *et al.* A room temperature low-threshold ultraviolet plasmonic nanolaser. *Nature Communications* **5**, 1-9 (2014).

16 Zhou, B., Shi, B., Jin, D. & Liu, X. Controlling upconversion nanocrystals for emerging applications. *Nat Nanotechnol* **10**, 924-936 (2015).

17 Gargas, D. J. *et al.* Engineering bright sub-10-nm upconverting nanocrystals for single-molecule imaging. *Nat Nanotechnol* **9**, 300-305 (2014).

18 Wu, S. *et al.* Non-blinking and photostable upconverted luminescence from single lanthanide-doped nanocrystals. *Proc Natl Acad Sci* **106**, 10917-10921 (2009).

19 Anderson, R. B., Smith, S. J., May, P. S. & Berry, M. T. Revisiting the NIR-to-visible upconversion mechanism in β-NaYF4:Yb3+,Er3+. *Journal of Physical Chemistry Letters* **5**, 36-42 (2014).

20 Zhu, H. *et al.* Amplified spontaneous emission and lasing from lanthanide-doped up-conversion nanocrystals. *Acs Nano* **7**, 11420-11426 (2013).
21 Fernandez-Bravo, A. *et al.* Continuous-wave upconverting nanoparticle microlasers. *Nat. Nanotechnol.* **13**, 572-577 (2018).
22 Haider, G. *et al.* A Highly-Efficient Single Segment White Random Laser. *Acs Nano* **12**, 11847-11859 (2018).
23 Ostrowski, A. D. *et al.* Controlled synthesis and single-particle imaging of bright, sub-10 nm lanthanide-doped upconverting nanocrystals. *Acs Nano* **6**, 2686-2692 (2012).
24 Tian, B. *et al.* Low irradiance multiphoton imaging with alloyed lanthanide nanocrystals. *Nat Commun* **9**, 3082 (2018).
25 Schuck, P. J., Willets, K. A., Fromm, D. P., Twieg, R. J. & Moerner, W. E. A novel fluorophore for two-photon-excited single-molecule fluorescence. *Chemical Physics* **318**, 7-11 (2005).
26 Grim, J. Q. *et al.* Continuous-wave biexciton lasing at room temperature using solution-processed quantum wells. *Nat Nanotechnol* **9**, 891-895 (2014).
27 Samuel, I. D. & Turnbull, G. A. Organic semiconductor lasers. *Chem Rev* **107**, 1272-1295 (2007).
28 Nielsen, M. P., Shi, X. Y., Dichtl, P., Maier, S. A. & Oulton, R. F. Giant nonlinear response at a plasmonic nanofocus drives efficient four-wave mixing. *Science* **358**, 1179-1181 (2017).
29 Yuan, P. *et al.* Plasmon enhanced upconversion luminescence of NaYF4:Yb,Er@SiO2@Ag core-shell nanocomposites for cell imaging. *Nanoscale* **4**, 5132-5137 (2012).
30 Sun, Q. C. *et al.* Plasmon-enhanced energy transfer for improved upconversion of infrared radiation in doped-lanthanide nanocrystals. *Nano Lett* **14**, 101-106 (2014).
31 Auguie, B. & Barnes, W. L. Collective resonances in gold nanoparticle arrays. *Phys Rev Lett* **101**, 143902 (2008).
32 Zou, S., Janel, N. & Schatz, G. C. Silver nanoparticle array structures that produce remarkably narrow plasmon lineshapes. *J Chem Phys* **120**, 10871-10875 (2004).
33 Yang, A. *et al.* Real-time tunable lasing from plasmonic nanocavity arrays. *Nature Communications* **6**, 6939 (2015).
34 Wang, D. Q. *et al.* Stretchable Nanolasing from Hybrid Quadrupole Plasmons. *Nano Lett* **18**, 4549-4555 (2018).
35 Liu, Q. *et al.* Single upconversion nanoparticle imaging at sub-10 W cm−2 irradiance. *Nat Photonics* **12**, 548-553 (2018).
36 Liu, Y. *et al.* Amplified stimulated emission in upconversion nanoparticles for super-resolution nanoscopy. *Nature* **543**, 229-233 (2017).
37 Wei, W. *et al.* Cross Relaxation Induced Pure Red Upconversion in Activator- and Sensitizer-Rich Lanthanide Nanoparticles. *Chem Mater* **26**, 5183-5186 (2014).

38 Tajon, C. A. *et al.* Photostable and efficient upconverting nanocrystal-based chemical sensors. *Opt Mater* **84**, 345-353 (2018).
39 Ma, R. M., Oulton, R. F., Sorger, V. J., Bartal, G. & Zhang, X. Room-temperature sub-diffraction-limited plasmon laser by total internal reflection. *Nat Mater* **10**, 110-113 (2011).
40 Teitelboim, A. *et al.* Energy Transfer Networks within Upconverting Nanoparticles Are Complex Systems with Collective, Robust, and History-Dependent Dynamics. *J. Phys. Chem. C* **123**, 2678-2689 (2019).
41 Chen, S. *et al.* Near-infrared deep brain stimulation via upconversion nanoparticle-mediated optogenetics. *Science* **359**, 679-684 (2018).

ACKNOWLEDGMENTS

This work was supported by the National Science Foundation (NSF) under DMR-1608258 and the Vannevar Bush Faculty Fellowship from DOD under N00014-17-1-3023. The work at the Molecular Foundry was supported by the Office of Science, Office of Basic Energy Sciences, of the U.S. Department of Energy under Contract No. DE-AC02-05CH11231. Portions of this research were supported by the Global Research Laboratory (GRL) Program through the National Research Foundation of Korea (NRF) funded by the Ministry of Science and ICT (no. 2016911815). The work used the Northwestern University Micro/Nano Fabrication Facility (NUFAB), which is partially supported by Soft and Hybrid Nanotechnology Experimental (SHyNE) Resource (NSF ECCS-1542205), the Materials Research Science and Engineering Center (DMR-1720139), the State of Illinois, and Northwestern University. A.T. was supported by the Weizmann Institute of Science - National Postdoctoral Award Program for Advancing Women in Science. We appreciate Dr. Francesco Scotognello for assistance with the ultrafast lasing measurements at the Molecular Foundry.

AUTHOR CONTRIBUTIONS

A.B. and D.W. contribute equally to this work. A.B. measured nonlinear optical properties, lasing emissions and coherence characteristics of upconverting nanoparticles and nanolasers, D.W. and J.G. fabricated plasmonic nanoparticle arrays, and D.W. characterized the linear optical

properties and modeled plasmon resonances and upconverting lasing. E.B. contributed to data analysis, A.T. and A.B. performed $g^{(2)}$ measurements, and C.T. contributed to upconverting nanoparticle synthesis. All authors analyzed the data, wrote and revised the manuscript.

COMPETING INTERESTS

The authors declare no competing interests.

Methods

Synthesis of core/shell UCNPs

β-$NaYF_4$ UCNP cores with 20% Yb^{3+}, 20% Er^{3+}, and 20% Gd^{3+} were synthesized as described[1,2] with minor modifications. $YbCl_3$ · H2O (0.080 mmol, 32 mg), YCl_3 (0.16 mmol, 31 mg), $ErCl_3$ (0.08 mmol, 22 mg), $GdCl_3$ (0.080 mmol, 21 mg), oleic acid (3.25 g), and 1-octadecene (ODE, 4 mL) were stirred in a 3-necked flask with an in-reaction thermocouple, heated at 110 °C under vacuum, and purged with N_2 every 15 min for 1 h. The dissolved lanthanides were then cooled under N_2, and sodium oleate (1.25 mmol, 382 mg), NH_4F (2.0 mmol, 74 mg), and ODE (3 mL) were added to the flask. The reaction mixture was stirred under vacuum at room temperature for 30 min and then heated at 317 °C for 45 min. The reaction flask was cooled to 40 °C with a strong stream of air, the product transferred to a 50-mL centrifuge tube, 10 mL of EtOH added, and the tube centrifuged at 3000 x g for 3 min. The supernatant was decanted and 3 mL of hexane used to wash the reaction flask was added to the pellet, which was dispersed by sonication. The tube was then centrifuged at 3000 x g for 3 min, the supernatant transferred to a new tube, 5 mL of EtOH was added, and the tube centrifuged again at 3000x g for 3 min. The pellet was dispersed in 1 mL of hexane, precipitated with 5 mL of EtOH two additional times, and the resulting pellet was dispersed in 15 mL of anhydrous hexane.

To overgrow inert 2-nm $NaYF_4$ shells on these 10-nm cores, we used a layer-by-layer protocol incorporating 20% Gd^{3+} to facilitate the growth of β -

phase morphology[3]. A hexane dispersion of 28 nmol of core UCNPs was added to a 3-neck, 50-mL flask and the hexane evaporated under N_2. Oleic acid (4 mL) and ODE (6 mL) were added and the flask was stirred at 70 °C for 1 hour under vacuum. In separate flasks, Ln oleates were prepared by heating YCl_3 (0.40 mmol, 78 mg), $GdCl_3$ (0.10 mmol, 26 mg), oleic acid (2 mL), and 1-octadecene (3 mL) at 110 °C for 1 h under vacuum; and sodium trifluoroacetate (1.20 mmol, 16 mg) was dissolved in oleic acid (3 mL) and stirred at room temperature for 1 hour under vacuum. The UCNPs flask was purged with N_2 and heated at 280 °C for 10 min, allowing the temperature to stabilize. Shell precursors were injected as in previous work[38], with sequential injections of lanthanide and Na/F precursors performed every 15 min. After four rounds of injections, the reaction was allowed to stir for an additional 30 min at 280 °C, and a strong stream of air to the flask was used for cooling. Core/shell UCNPs were isolated and stored using the same protocol for core UCNPs. Final TEM diameters were measured to be 13.9 ± 0.8 nm (Supplementary Fig 1).

Nanoparticle characterization

For TEM imaging, stock solutions of oleate-capped UCNPs were diluted 100-fold in hexane and 10 µL was adsorbed onto a carbon film/ holey carbon, 400 mesh copper grid (Ted Pella). The grid was wicked of excess hexane and allowed to dry in the hood. Standard TEM images were taken with a FEI Tecnai TEM or Philips CM200/FEG in SEM mode. Size statistics were acquired for approximately 100 nanoparticles using ImageJ software. Incoherent Z-

contrast images were acquired using a high angle annular dark field detector (HAADF, Fischione) on the TEAM I aberration-corrected electron microscope (Thermo Fischer Scientific) in scanning transmission (STEM) mode, with a primary beam energy of 300 keV. Core/shell structures were characterized by incoherent Z-contrast imaging with a high angle annular dark field detector (HAADF) on an aberration-corrected scanning transmission electron microscope (STEM). Core/shell structures are apparent based on Z-contrast with an abrupt change in the intensity of the atomic columns corresponding to differences in Ln^{3+} content between core and shell, a transition not seen in the UCNP cores.

Preparation of plasmonic nanopillar arrays

Ag nanopillars are in a cylindrical shape (diameter 80 nm, height 50 nm) and scalable up to cm^2 by large-scale nanopatterning processes. We made these samples by thermal metal deposition, and no annealing process was involved. Arrays of Ag nanopillars on fused silica were fabricated with a soft nanofabrication process referred to as PEEL[4]. Briefly, we generated periodic photoresist posts on Si wafers by phase-shifting photolithography with controlled post size. The patterns were then transferred into free-standing Au nanohole films after Cr deposition, removal of photoresist posts, etching through the Si nanoholes and lift-off of Au film. Finally, we created Ag nanopillar arrays by metal deposition through the hole-array mask on a transparent substrate and then removal of the mask. A 2-nm Cr layer was deposited in-between for better adhesion between Ag nanopillars and fused

silica. Later for protection of these nanopillars, we used atomic layer deposition to deposit 5 nm Al_2O_3 around the nanopillar surface.

Preparation of lanthanide-based nanoparticles plasmon nanolasers

Solution-processed UCNPs were drop cast on top of Ag nanopillar arrays (diameter d = 80 nm, height h = 50 nm). The thickness of the coating can be controlled with the concentration of the nanocrystals in solution. The drop-cast film thickness was ca. 150 nm for the devices discussed here. The measured transmission spectra suggested that sharp lattice plasmon resonances were preserved after coating Ag nanopillars with Yb^{3+}/Er^{3+} UCNP emitters.

Confocal microscopy and spectroscopy

For direct UCNP excitation, a dispersion of nanoparticles was added to a glass coverslip and placed on an inverted confocal microscope (Nikon). A 980-nm laser (ThorLabs) was directed into the back aperture of a 0.1 NA 4× Objective (Nikon), and focused directly on the sample. The emitted light was collected back through the same objective, filtered by one 496-nm long-pass and one 745-nm short-pass (SP) filter (Semrock, Inc. Brightline multiphoton filter), in addition to a 720SP dichroic and sent to an LN_2-cooled CCD-equipped spectrometer (Princeton Instruments). The same confocal microscope was used for excitation of the upconverting plasmon nanolaser and spectroscopy studies of laser modes. Different gratings are available in the dispersion system, namely 150 grooves/mm and 600 grooves/mm, providing different spectral resolution and dynamic ranges. The resolution of

the spectrometer is 0.1 nm, which could be improved slightly by closing the slit of the spectrometer at a cost of collection efficiency. For power dependence measurements for the evaluation of lasing action, a neutral density wheel with a continuously variable density was used, synchronized with the collection system and automatically rotated by an Arduino-controlled rotator. Powers were simultaneously recorded by a Thorlabs power meter by using a glass coverslip to reflect ~10% of the incoming flux. The powers were in-line recorded in H5-files as metadata for each independent file.

Wide-field imaging

For wide-field imaging, a CMOS Andor Neo 5.5 camera was attached to the microscope without going through the confocal optical pathway. Instead, the signal was collected laterally on one of the external side ports of the microscope.

Photon statistics

A second-order correlation measurement was implemented using a Hanbury-Brown and Twiss (HBT) setup with a 50/50 beam splitter and 2 MPD detectors. The $g^{(2)}$ optical second-order cross correlation is defined as:

$$g^{(2)}(\tau)=\langle I_{det1}(t) \bullet I_{det2}(t+\tau)\rangle$$

where I_{det1} (t) and I_{det2} (t) are the signal intensities measured at the two detectors (the two discrete photon streams collected by the two channels). The brackets denote the expectation value and t and τ are the photon arrival time and delay. The counts in the $g^{(2)}$ histogram are the number of photon

pairs detected for different delays using the two detectors (which means it should vary with the measurement length, selected bin size and signal intensity). The normalized $g^{(2)}$ is:

$$g^{(2)}¿\frac{\langle I_{det1}(t)\bullet I_{det2}(t+\tau)\rangle}{\left(\langle I_{det1}(t)\rangle\bullet\langle I_{det2}(t+\tau)\rangle\right)}$$

which is the normalization by division of the mean signal of the two detectors.

The second order correlation has been used to evaluate the photon statistics for the upconverting plasmon nanocavity array, producing upconverted lasing by coupling these nanocavity arrays with Yb^{3+} and Er^{3+} ions doped in a $NaYF_4$ matrix, which are able to upconvert near-infrared 980 nm excitation wavelength to red (ca. 660) nm visible emission from the Er. The emission at ca. 660 nm coupled resonantly with the engineered plasmon nanocavity array, and when the excitation power was above the threshold, lasing appeared selected from Er^{3+} emission at ca. 660 nm. The emission spectra show that the nanocavity mode modifies the Er^{3+} spontaneous emission even at low pump powers, funneling energy into the preferential mode, which increases in intensity and narrows with increased pump power. The plot of emission intensity versus pump power shows that its intensity and linewidth are power dependent with a P_{Th}~ 30-70 W/cm^2 for CW pumping and P_{Th}~ 32-300 W/cm^2 average power for pulsed pumping conditions.

The plasmon lasers were measured at above-threshold excitation pump powers of 112 W/cm^2 for CW and 230 W/cm^2 for pulsed pumping at 980 nm.

Supplementary Fig. 10 depicts the $g^{(2)}$ histogram for the upconverted lasing at ca. 660 nm for above-threshold powers (CW and pulsed pumping schemes), showing that the normalized $g^{(2)}$ function is 1 for both pumping schemes. This demonstrates that there is no temporal correlation between the emitted photons, which is a signature of CW lasing. Below and above threshold measurements of the laser emission yield a small photon bunching for below laser thresholds at $g^{(2)}(t=0)$ attributed to amplified spontaneous emission (ASE); a comparison to Er^{3+} spontaneous emission is added to the plot in Supplementary Fig. 11. As a reference, the second order optical cross correlation $g^{(2)}$ of the 80 MHz chameleon laser at 800 nm was measured with the same detector configuration. Supplementary Fig. 12 depicts the $g^{(2)}$ histogram of the chameleon laser at 800 nm, showing the pulsing of the 80 MHz laser with bunching peaks rising every 12.5 ns corresponding to the laser repetition rate (bunching peaks every 12.5 ns corresponds to the laser pulse train). Note that there is no bunching peak recorded for the upconverting plasmon nanocavity laser, which instead shows photon statistics typical of CW lasing emission. A Poissonian distribution is not sufficient to indicate CW lasing behavior, since lanthanide spontaneous emission also exhibits this. However, the highly nonlinear scaling with power shows slopes as high as 10, which agrees with our upconverting lasing modeling, and the simultaneous mode narrowing experienced at threshold powers indicates lasing behavior that happens in a CW fashion.

Finite-difference time-domain (FDTD) simulations

FDTD calculations with commercial software (FDTD solution, Lumerical Inc., Vancouver, Canada) were used to simulate the linear optical properties of Ag nanopillar arrays. The optical constant of Ag was taken from Johnson and Christy measurements (400–1000 nm). A uniform mesh size of 4 nm (x, y and z) was used to ensure the accuracy of electric and magnetic field calculations within the metal nanopillars.

Simulation of upconverting nanolasing was performed by home-built Matlab codes, where a six-level one-electron model was integrated for modeling Yb^{3+}/Er^{3+}-co-doped UCNPs. The narrow lattice plasmon resonance provides selective enhancement only for the Er^{3+} red emission without directly affecting other energy transfer processes, and hence, we could use a simplified six-level model to approximately describe the upconverting lasing process (Supplementary Figs. 13-15). In the semi-quantum system, we set the Ag nanopillar size d = 80 nm and height h = 50 nm, pump wavelength at λ_a = 980 nm, emission at λ_e = 660 nm and index n = 1.42, close to experimental conditions. The decay lifetimes were set as $t_{54} = t_{10} = 10$ fs, t_{41} = 0.1 ns, and $t_{50} = t_{32} = t_{30} = 1$ ns. We initially pumped the six-level system from the ground state (population density $N_0 = 1$, $N_1 = N_2 = N_3 = N_4 = N_5 = 0$) and collected all emitted flux with a plane monitor placed 0.3 μm away on top of the nanopillars. Er^{3+} emitter concentration was C = 3 mM. The whole simulation is within ~1 ps, and time-dependent evolution of population density at different energy levels was tracked to probe the characteristic population inversion for lasing action.

DATA AVAILABILITY

The data that support the findings of this study are available from the corresponding authors upon reasonable request.

References

42 Tajon, C. A. *et al.* Photostable and efficient upconverting nanocrystal-based chemical sensors. *Opt Mater* **84**, 345-353 (2018).

43 Tian, B. *et al.* Low irradiance multiphoton imaging with alloyed lanthanide nanocrystals. *Nat Commun* **9**, 3082 (2018).

44 Levy, E. S. *et al.* Energy-Looping Nanoparticles: Harnessing Excited-State Absorption for Deep-Tissue Imaging. *Acs Nano* **10**, 8423-8433 (2016).

45 Henzie, J., Lee, M. H. & Odom, T. W. Multiscale patterning of plasmonic metamaterials. *Nature nanotechnology* **2**, 549-554 (2007).